Published in final edited form as:
Inorg Chem. 2014 February 17; 53(4): 1916–1924. doi:10.1021/ic402194c.

Metal-Organic Frameworks as Sensory Materials and Imaging Agents

Demin Liu, **Kuangda Lu**, **Christopher Poon**, and **Wenbin Lin**
Department of Chemistry, University of Chicago, 929 E. 57th Street, Chicago, IL 60637

Wenbin Lin: wenbinlin@uchicago.edu

Abstract

Metal-organic frameworks (MOFs) are a class of hybrid materials self-assembled from organic bridging ligands and metal ion/cluster connecting points. The combination of a variety of organic linkers, metal ions/clusters, and structural motifs can lead to an infinite array of new materials with interesting properties for many applications. In this Forum article, we discuss the design and applications of MOFs in chemical sensing and biological imaging. The first half of this article focuses on the development of MOFs as chemical sensors by highlighting how unique attributes of MOFs can be utilized to enhance sensitivity and selectivity. We also discuss some of the issues that need to be addressed in order to develop practically useful MOF sensors. The second half of this article focuses on the design and applications of nanoscale metal-organic frameworks (NMOFs) as imaging contrast agents. NMOFs possess several interesting attributes, such as high cargo loading capacity, ease of post-modification, tunable size and shape, and intrinsic biodegradability, to make them excellent candidates as imaging contrast agents. We discuss the use of representative NMOFs in magnetic resonance imaging (MRI), X-ray computed tomography (CT), and optical imaging (OI). Although still in their infancy, we believe that the compositional tunability and mild synthetic conditions of NMOF imaging agents should greatly facilitate their further development for clinical translation.

Introduction

Metal-organic frameworks (MOFs), also called porous coordination polymers, are an emerging class of crystalline porous materials composed of inorganic metal ions or clusters connected by polydentate organic linker ligands.

Unlike traditional zeolites, which are comprised of SiO_4 and AlO_4 building blocks, the organic linkers in MOFs can be readily varied to allow for direct manipulation of their physical and chemical properties. Furthermore, MOFs are typically synthesized under mild conditions so a large variety of molecular functionalities can be rationally designed and incorporated into MOFs to impart desired properties for potential applications. Over the past 15 years, a large number of MOFs have been tailor-made for applications in many areas, including catalysis,[1–5] gas separation and storage,[6–9] nonlinear optics,[10] light-harvesting,[11]

Correspondence to: Wenbin Lin, wenbinlin@uchicago.edu.

and drug delivery.[12–14] MOFs have also recently been explored as sensory materials and imagining agents.

Chemical sensors have long been used in many applications, such as industrial hygiene,[15, 16] quality control,[16, 17] emission monitoring,[18–20] and clinical diagnostics.[21, 22] Ideal chemical sensors should be highly sensitive to analytes of interest, and yet remain unperturbed by other molecules or materials that may be present. In addition, the sensors must be stable so they can be stored for a long period of time and can be reused for many times to reduce costs. The most investigated and commercially produced chemical sensors are inorganic[23, 24] or organic semiconductor films[25, 26] with typically ill-defined structures. Despite their versatile utility and commercial success, existing classes of chemical sensors can have limited sensitivity and selectivity. The crystalline and porous nature of MOFs endows them unique properties and offers several potential advantages over existing materials in chemical sensing. First, highly porous structures of MOFs can allow enhanced uptake of molecules or ions into their pores due to preferential interactions between molecules or ions and the pore surfaces. Such a pre-concentration effect can enhance the sensitivity of the sensing moieties in MOFs. Second, the well-defined pore and channel structures of MOFs can exclude certain species to provide an additional mechanism for selective sensing that might not be operative in existing sensory materials. Third, the reduced conformational flexibility of sensing moieties in the frameworks of MOFs can also contribute to enhanced selectivity in molecular sensing. The first half of this Forum article summarizes recent studies of MOFs as chemical sensors. We attempt to illustrate unique attributes of MOF sensors using literature examples and to highlight the potential advantages of MOFs over existing materials in chemical sensing.

When scaled down to the nano-regime, many of bulk sensory materials can also be used as imaging agents for various diseases. Nanoparticles, in particular those of 20–200 nm in diameter, have several advantages over small molecule imaging agents, such as high payloads, tunable sizes, tailorable surface properties, and improved pharmacokinetics.[27–30] Nanoparticles tend to have increased tumor uptake due to the enhanced permeability and retention (EPR) effect stemming from leaky neovasculatures and ineffective lymphatic drainage that are characteristic of tumors.[31] The accumulation of nanoparticles in tumors can be further enhanced by surface conjugation of cancer-specific ligands.[32, 33] The Lin group first recognized the potential of nanoscale metal-organic frameworks (NMOFs) as contrast agents for biomedical imaging. Prior to NMOFs, nanoparticle imaging agents are either purely inorganic or organic. It was hypothesized that NMOFs can combine attractive features of both inorganic and organic nanomaterials, such as chemical diversity, high loading capacity, and intrinsic biodegradability, to offer an entirely new class of imaging contrast agents. In the past few years, NMOFs have been explored as potential contrast agents for a number of imaging modalities, including magnetic resonance imaging (MRI), X-ray computed tomography (CT) imaging, and optical imaging (OI). The second half of this forum discusses potential use of NMOFs in biomedical imaging. We try to highlight recent literatures on designing NMOFs for various imaging applications.

MOFs as Sensors and Sensory Materials

A chemical sensor must have desired selectivity, sensitivity, response times, material stability, and reusability. MOFs exhibit unique characteristics to become excellent chemical sensors. The porous nature of MOFs can potentially preconcentrate the analytes to achieve enhanced sensitivity. Meanwhile, the pores and channels can provide an ideal environment to accommodate the analyte molecules and to induce specific recognition. In the examples provided below, the selectivity of MOF sensors is derived from 1) channel size exclusion; 2) specific coordination or hydrogen bonding of analytes to the framework; 3) analyte-specific signal response; 4) host-guest chemistry in the MOF cavity; 5) the chirality of the framework. In addition, amplified quenching was recently demonstrated with phosphorescent MOFs,[34] which provides an additional mechanism to significantly enhance the sensitivity of MOF sensors. Although MOF materials display outstanding stimulus response (sensing) properties, few of them have been used to construct sensing devices to date. Processing MOF materials into thin films[35] or nanocrystals[36, 37] remains a hurdle for converting sensory MOF materials into functional sensing devices.

Size-dependent sensing of gas molecules

Lu and Hupp reported a ZIF-8 vapor sensor which displays chemical selectivity resulting from the small portal size of the cavities.[35] The ZIF-8 sensor was obtained in a thin-film form of controllable thickness (Figure 1a) by immersing glass or silicon slides in a freshly prepared methanolic solution of 2-methylimidazole and $Zn(NO_3)_2$ at room temperature. The sensing is based on Fabry-Pérot interference which occurs when incident light reflect off two parallel surfaces separated by a distance, *l*, on the order of the wavelength of light. The wavelengths of the interference peaks can be determined by the formula below:

$$m\lambda = 2nl \quad (1)$$

where *m* is an integer and *n* is the thin film's refractive index.

When polarizable molecules enter the cavity, the overall reflective index will increase, resulting in red shifts of the interference peaks. The shift can be determined quantitatively as manifested by propane/N_2 flow test at different propane partial pressures (Figure 1b, d). Although the response is not molecule-specific, the MOF sensor does display some chemical selectivity based on its channel size and the hydrophobic nature of the framework. For example, linear n-hexane is readily sensed while cyclohexane is not, probably due to the size exclusion by the small portal size for ZIF-8 cavities. The sensor is unresponsive to water vapor but can detect ethanol. The ethanol-concentration-dependent responses were used to determine ethanol concentrations in ethanol/water mixtures with the sensor response saturating at ca. 40% ethanol (Figure 1c, e).

Such effects were also observed in other vapor-sensing MOFs. Li and coworkers reported a microporous $[Zn_2(bpdc)_2(bpee)]$ MOF (bpdc=4,4'-biphenyldicarboxylate; bpee=1,2-bipyridylethene) for explosive sensing.[38] The framework fluorescence can be quenched by analogs of explosive molecules such as 2,4-dinitrotoluene (DNT) and 2,3-dimethyl-2,3-dinitrobutane (DMNB) through a redox quenching mechanism (Figure 2). The pore size

confinement leads to the enhancement of DMNB quenching, as is reflected by the relatively small difference in the quenching percentages for nitrobenzene and DMNB despite the fact that nitrobenzene should have elicited larger fluorescence quenching owing to its much higher vapor pressure, more favorable reduction potential, and stronger π–π interactions with the framework.

MOFs can also be combined with other sensing structures to enhance sensor performances. For instance, by coating noble-metal nanoparticles with MOFs, both selectivity and sensitivity of gas sensing could be enhanced dramatically. [26, 29]

Luminescent ion sensing via coordination or hydrogen bonding to MOFs

Vacant binding sites in the MOF framework can be utilized to elicit selectivity in ion sensing. For metal cation sensing, Lewis basic centers within porous MOFs are desired. Envisioning preferential binding of Ln^{3+} ions to carboxylate oxygen over pyridyl nitrogen atoms, Chen et al. prepared an Eu-pdc MOF (pdc= pyridine-3,5-dicarboxylate) with dangling Lewis basic pyridyl sites for the sensing of metalions (Figure 3).[39] After activation in DMF solutions of the metal ions, the $[Eu(pdc)_{1.5}]$·DMF MOF shows luminescence quenching response selectively to ions such as Cu^{2+}, Mn^{2+} or Co^{2+}. The quenching is suggested to result from the weak binding of pyridyl nitrogen atoms to M^{2+}, which reduces the energy transfer efficiency of the pdc organic linkers to the f–f transitions of Eu^{3+}.

Jiang et al. used a different route for cation recognition.[40] They synthesized $[Pb_2(bco)_2(bipy)]$ (bco=1,5-bis(m-carboxyphenoxy)-3-oxapentane and bipy=4,4'-bipyridine), from which the weakly coordinating bipy can be leached out post-synthetically (Figure 4). After removal of the bipy ligand, the resulting hydrophilic channels can reversibly encapsulate $[Ln(H_2O)_8]^{3+}$ ions. The confined oxygen-rich environment induces host-guest O-H···O hydrogen-bonding interactions that reduces the O-H vibration coupling on $[Ln(H_2O)_8]^{3+}$ ions, resulting in much higher emission intensity after entrapment.

Hydrogen bonding was utilized by Chen et al. for anion recognition and sensing with MOFs. They reported a luminescent Tb(BTC)·G (BTC=benzene-1,3,5-tricarboxylate, G=guest solvent) MOF as an anion sensor which exhibits high sensitivity and selectivity for fluoride (Figure 5).[41] The luminescence intensity of the Tb(BTC)·methanol was enhanced after anion incorporation: the F^- incorporated MOF showed four times stronger luminescence signal than the non-F^- counterpart (Figure 5b). The luminescence enhancement was proposed to result from hydrogen bonding of F^- to terminal methanol, as indicated by F^-···O (from methanol) distances of 2.78 to 3.24 Å (Figure 5a). Such strong hydrogen bonding interaction alleviates the quenching effect of the O-H bond stretching vibrations, thereby leading to luminescence enhancement. A recent report by Song and coworkers described luminescence turn-on sensing of DMF vapor by a Eu-MOF using a similar strategy.[30]

Analyte-specific signal response for selective sensing

For accurate and quantitative sensing, a sensory material that responds to specific molecules is desired. Lin and coworkers reported a highly phosphorescent MOF series based on $Ir(ppy)_3$ (ppy=2-phenylpyridine) derivatives which can be readily quenched by oxygen (Figure 6).[42] Linear Stern-Völmer plots of I_0/I vs. $p(O_2)$ (oxygen partial pressure) were

obtained and the reversibility of the luminescent quenching was evaluated by examining the emission intensity change when the $p(O_2)$ was cycled between 0 and 0.1 atm (Figure 6c, d). It was found that permanent porosity is required for kinetically reversible O_2 quenching. In this sensing scheme, the microporosity of MOFs can impart additional selectivity as large interfering molecules are excluded from quenching the MOF luminescence. Chen and coworkers adopted the same principle to design Ru-doped azolate MOF for oxygen sensing.[43, 44]

Host-guest chemistry in entangled frameworks for molecular decoding

Although many sensory MOFs have been reported, few of them can distinguish similar analytes due to the fact that these MOF materials transduce the intensity of only one kind of signal. An interesting MOF system was developed by Kitagawa and coworkers to decode multiple analytes by transducing a particular host–guest interaction into corresponding luminescent signals (Figure 7a).[45] $[Zn_2(bdc)_2(dpNDI)]_n$ (bdc=1,4-benzenedicarboxylate; dpNDI = N,N'-di(4-pyridyl)-1,4,5,8-naphthalenediimide) possesses an entangled structure, which is believed to be crucial for signal transduction. Upon uptaking aromatic volatile organic compounds (VOCs), the entangled framework shows a crystal-to-crystal transition from distorted to non-distorted structure, accompanied by a strong analyte-specific fluorescence signal (Figure 7b–d). Two analyte-specific fluorescence turn-on mechanisms were proposed: charge-transfer emission and heavy atom induced phosphorescence enhancement. The signal response is enhanced by the host-guest interaction, but non-linear with respect to the concentration of the guest molecules.

A Chiral MOF for enantioselective sensing

Rapid determination of enantiomeric excesses (ee) of organic compounds has become a bottleneck in identifying efficient means to produce chiral molecules. Lin and coworkers hypothesized that chiral MOFs can provide an excellent platform for enantioselective sensing by taking advantage of the confinement effect of the framework and the conformational rigidity of the sensing moieties to enhance stereoselectivity.[46] A BINOL based chiral porous MOF $[Cd_2(L)(H_2O)_2]\cdot 6.5DMF\cdot 3EtOH$ [LH_4=(R)-2,2'-dihydroxy-1,1'-binaphthyl-4,4',6,6'-tetrakis- (4-benzoic acid); DMF=N,N-dimethylformamide] was tested as an enantioselective sensor for amino alcohols via fluorescence quenching (Figure 8a).[46] The MOF gives much higher detection sensitivity (up to 1000 fold) and greater enantioselectivity when compared with the homogeneous control. For 2-amino-3-methyl-1-butanol (AA), the MOF has a quenching ratio (QR = $k_{SV}(S)/k_{SV}(R)$) of 3.12 while the homogeneous control has a quenching ratio of 1.21 (Figure 8b). The increase of sensitivity is believed to result from a pre-concentration effect, as proven by the determination of the solubility partition coefficient in MOF and acetonitrile by gas chromatographic analyses. The enantioselectivity enhancement of the AA substrate is likely caused by the steric confinement of the MOF cavity. The MOF sensor was also shown to be capable of determining the enantiomeric ratio of a mixture of (*S*)- and (*R*)-AA in predetermined proportions by comparing with the calibration curve which exhibits a linear relationship between the fluorescence signal and the ee of the analyte. This work demonstrates that chiral porous MOFs can provide an excellent platform for developing practically useful chiral sensors.

MOFs as Imaging Agents

Despite enormous progress in our fundamental understanding of cancer biology, the mortality rate for most cancers has remained unchanged over the past 2–3 decades.[47] It has long been recognized that early detection is the key for effective treatment of cancer. Unfortunately, many patients are still diagnosed at late stages of cancer due to limited sensitivity and selectivity of current diagnostic techniques.[48] Conventional diagnostic agents, such as Gd^{3+} chelates for MRI and iodinated aromatic molecules for CT imaging, are limited by their short blood circulation times and nonspecific biodistribution. In an attempt to overcome these limitations, various nanoparticle platforms have been developed for cancer diagnostics. Nanoparticles in the size range of 10–100 nm provide several potential advantages over conventional small molecule agents, including extension of circulating half-lives, passive accumulation at tumor sites due to the enhanced permeability and retention (EPR) effect, active targeting of cancer cells, and improved safety profiles.[49]

Lin and coworkers have developed systematic strategies to scale down MOFs to the nano-regime to form crystalline nanoscale metal-organic frameworks (NMOFs) or amorphous nanoscale coordination polymers (NCPs) for imaging and drug delivery.[50] A variety of different techniques, including nanoprecipitation,[13] solvothermal,[51] reverse microemulsion,[52] and surfactant-templated solvothermal reactions, have been developed to synthesize NMOFs and NCPs.[53] Biomedically relevant agents were loaded into NMOFs or NCPs using two general strategies, either by integrating active agents into the frameworks directly (Scheme 1a)[54, 55] or by loading active agents into the pores and channels of the NMOFs (Scheme 1b).[14, 51, 56–58] The surfaces of as-synthesized NMOF and NCP particles were modified with a thin shell of silica[59–61], organic polymers (e.g., polyethylene glycol, polyvinylpyrrolidone),[13, 54, 61, 62] or lipid bilayers[12, 63] in order to enhance their stabilities, fine-tune their physicochemical properties, and impart additional biocompatibility and functionality. A number of NMOFs and NCPs have been tested as biomedical imaging agents *in vitro* and *in vivo*.

NMOFs for magnetic resonance imaging

Magnetic resonance imaging (MRI) is a non-invasive imaging technique whereby images are generated based on the nuclear magnetic resonance (NMR) signals of the water proton (^1H) nuclei in a specimen. MRI is a powerful imaging modality with high spatial resolution and depth of penetration. However, their low sensitivity requires that a relatively large amount of contrast agent be administered to provide adequate MR contrast. Lin and coworkers explored NMOFs as MRI contrast agents by taking advantage of large payloads of paramagnetic metal ions NMOFs can carry. Both Gd^{3+}- and Mn^{2+}-containing NMOFs were shown to serve as excellent T_1-weighted MRI contrast agent with large per metal- and per particle-based MR relaxivities.[53, 54]

NMOFs of $Gd(BDC)_{1.5}(H_2O)_2$ and $[Gd(1,2,4\text{-}BTC)(H_2O)_3]H_2O$ were synthesized by stirring an optically transparent microemulsion of $GdCl_3$ and bis(methylammonium)benzene-1,4-dicarboxylate (BDC) or tri-(methylammonium)benzene-1,2,4-tricarboxylate (1,2,4-BTC) in the cationic cetyltrimethylammonium bromide (CTAB)/isooctane/1-hexanol/water system.[52] Surfactant

molecules played an important role in defining NMOF morphologies. By varying the water/surfactant molar ratio (W value) and reaction time, distinct particle morphologies were obtained. This reverse microemulsion-based synthetic methodology was general and applied to many other NMOF and NCP systems. Extraordinarily large longitudinal relaxivity ($r1$ = 1.6×10^7 $mM^{-1}s^{-1}$) and transverse relaxivity ($r2 = 2.5\times10^7$ $mM^{-1}s^{-1}$) on a per mM of nanoparticle basis were obtained for $Gd(BDC)_{1.5}(H_2O)_2$ due to large amount of Gd^{3+} centers carried by each particle (Figure 9a). Highly luminescent Eu- and Tb-doped $Gd(BDC)_{1.5}(H_2O)_2$ nanoparticles were also synthesized by adding a small amount (5 mol%) of Eu^{3+} or Tb^{3+} into the Gd NMOF synthesis to render them potentially useful as multimodal imaging agents (Figure 9b).

The abovementioned Gd NMOFs were modified with polyvinylpyrrolidone (PVP) and then coated with a thin shell of silica in order to control the release of Gd^{3+} ions.[61] Thickness of the silica shell could be controlled precisely by tuning the base concentration and reaction time. Silica coatings on nanoparticles can improve water dispersibility, biocompatibility, and the ability to further functionalize the shell through co-condensation of siloxy-derived moieties. It was shown that the silica coating retarded the release of cargos from NMOFs, presumably as a result of the slow diffusion rate of metal and organic constituents through the silica shell. To illustrate the utility of NMOF-based core-shell nanostructures, Eu-doped $Gd(BDC)_{1.5}(H_2O)_2@SiO_2$ was prepared and the silica surface was further functionalized with a silylated Tb-EDTA monoamide derivative. Ratiometric luminescence sensing of dipicolinic acid (DPA), a chemical marker for anthrax spore, with a detection limit as low as 48 nM was achieved due to the optical signals generated from the binding of DPA to Tb complexes on the nanoparticle surface.

Lin and coworkers also reported the synthesis of two new Gd NMOFs, $[Gd_2(bhc)(H_2O)_6]$ (bhc=benzenehexacar-boxylate) and $[Gd_2(bhc)(H_2O)_8](H_2O)_2$ using a surfactant-assisted technique at elevated temperatures.[53] The two different NMOFs based on the identical Gd and bhc building blocks result from different metal-ligand coordination modes. The potential of these NMOFs as MRI contrast agents was demonstrated by a relaxivity study wherein a modest $r1$ of 1.5 $mM^{-1}s^{-1}$ and an impressive $r2$ of 122.6 $mM^{-1}s^{-1}$ on a per-Gd basis were obtained. Due to the high Gd payloads in these particles, the $r1$ and $r2$ relaxivities on a per-particle basis were determined to be 8.36×10^5 $mM^{-1}s^{-1}$ and 6.83×10^7 $mM^{-1}s^{-1}$, respectively.

The toxicity associated with Gd^{3+} leaching hinders the *in vivo* applications of Gd NMOFs as MRI contrast agents. To overcome this issue, Lin and coworkers designed NMOFs using Mn^{2+} as the metal-connecting points to afford T_1-weighted MR-enhancing agents that are more biocompatible and less toxic.[54] $Mn(BDC)(H_2O)_2$ and $Mn_3(BTC)_2(H_2O)_6$ were synthesized by reacting terephthalic acid (BDC) and trimesic acid (BTC) with $MnCl_2$ in reverse-phase microemulsions, respectively.[54] These particles were coated with a thin silica shell and their surfaces were subsequently functionalized with a cyclicarginine-glycine-aspartate (RGD) peptide for tumor-specific targeting. The Mn NMOFs were shown to be highly efficient T_1-weighted MR contrast agents *in vitro* due to their ability to carry large payload of Mn^{2+} and subsequent release of Mn^{2+} upon NMOF decomposition. Increased

uptake of the cRGD targeted particles was confirmed by *in vitro* MRI, confocal microscopy, and ICP-MS studies (Figure 10).

Iron-based NMOFs of the MIL structures were shown to be efficient contrast agents for T_2-weighted MR imaging.[14] The PEGylated MIL-88 nanoparticles exhibited an *r*2 relaxivity of 50 $mM^{-1}s^{-1}$ at 9.4 T. *In vivo* MR imaging of Wistar female rats 30 mins after nanoparticle injection showed enhanced contrast in liver and spleen (Figure 11). In a separate study where biodistribution, metabolism and excretion of iron-based NMOFs was investigated in rats after i.v. injections, Horcajada and coworkers showed that iron-based NMOFs did not lead to any acute toxicity in rats after high doses of these nanoparticles, thus supporting the potential usage of iron-based NMOFs for biomedical applications.[64]

NMOFs for computed tomography imaging

By incorporating high Z element building blocks, NMOFs have also been tested as contrast agents for X-ray computed tomography (CT) imaging.[55] Iodinated NMOFs of the formulae$[Cu(I_4\text{-BDC})(H_2O)_2]\cdot 2H_2O$ and $[Zn(I_4\text{- BDC})(EtOH)_2]\cdot 2EtOH$ were prepared using 2,3,4,5,6-tetraiodo-1,4-benzenedicarboxylate (I_4-BDC) as the bridging ligands and Cu^{2+} and Zn^{2+} as the metal connecting points. These NMOFs carry exceptionally high iodine content (up to 63 wt%). As shown in Figure 12, phantom studies indicated that these particles have X-ray attenuation coefficients comparable to that of the molecular contrast agent (Iodixanol). NMOFs thus provide a novel platform for designing efficient CT contrast agents by incorporating iodinated bridging ligands.

More recently, Lin and coworkers prepared Zr-BDC and Hf-BDC NMOFs of the UiO-66 structure. These particles carry 37 wt% Zr and 57 wt% Hf, respectively. The Hf NMOF was twice as efficient in attenuating X-rays as Iodixanol, resulting from the higher X-ray attenuation coefficient of Hf compared to I. The Hf-BDC NMOF was further coated with silica and poly(ethylene glycol) (PEG), and examined as a contrast agent for *in vivo* CT imaging of mice.[65] Enhanced attenuation in the liver (+131 HU) and spleen (+86 HU) was observed in mice 15 min after i.v. injection (Figure 13). The NMOF platform thus provides a promising strategy for incorporating high loadings of heavy elements into nanoparticles that can be surface-functionalized for enhanced biocompatibility and in vivo performance.

NCPs for Optical Imaging

Optical imaging (OI) is another powerful imaging modality for detecting tumor and other diseased tissues due to their noninvasive nature and higher sensitivity compared to MRI and CT. Organic-dye loaded nanoparticles and luminescent quantum dots are two major nanoprobes for optical imaging. The former can suffer from self-quenching and photobleaching whereas the latter can have high toxicity. To overcome these problems, Lin and coworkers hypothesized that highly luminescent nanoparticles can be constructed from metal complexes whose luminescence originates from the triplet states with long lifetimes and large Stokes shifts.[66] Such luminescent nanoparticles will not undergo self-quenching even at very high dye loadings. Phosphorescent NCPs were synthesized using a carboxylic acid derivative of $Ru(bpy)_3^{2+}$ (bpy is 2,2'-bipyridine) as a bridging ligand and Zn^{2+} or Zr^{4+} metal-connecting points (Figure 14a).[66] The Zn and Zr NCPs have extremely high

$Ru(bpy)_3^{2+}$ dye loadings of 78.7% and 57.4%, respectively. The Zr NCP was further stabilized with a thin shell of amorphous silica to prevent rapid dye release from the nanoparticles, and the biocompatibility and targeting efficiency of the NCP/silica core-shell nanostructures were further improved by coating with PEG and PEG-anisamide. Enhanced contrast and uptake was confirmed by laser scanning confocal fluorescence microscopy and particle uptake studies using H460 lung cancer cells (Figure 14b).

Kimizuka and coworkers synthesized NCPs based on nucleotide and lanthanide ion building blocks.[67] Fluorescent dyes and many other functional molecules can be readily encapsulated into nanoparticles during the NCP synthesis. Fluorescent dyes in these nanoparticles have higher quantum yields when compared to free dyes in solid form with a single exponential decay, showing that guest molecules are monomerically wrapped in the network. Adsorption of polyelectrolytes on nanoparticles surfaces was shown to improve their water solubility and biocompatibility. However, biodistribution study using fluorescence imaging and ICP-MS showed that these particles were rapidly captured by liver in mice after i.v. injection. Nevertheless, the adaptive nature of this NCP platform provides a facile means for incorporating and delivering functional cargoes.

Conclusion and Outlook

As outlined in this Forum article, MOFs have emerged as a promising platform for chemical sensing and biological/biomedical imaging. Several unique properties of MOFs have been utilized for their specific recognition of small molecules or ions in chemical sensing. The tunability of MOF synthesis should allow the design of next generation of MOF sensors that exhibit excellent sensitivity, by taking advantage of pre-concentration effect of the pores and channels in MOFs and enhanced selectivity, as a result of well-defined pores and channels and the framework rigidity in MOFs. In order to move MOF sensors into the realm of practical applications, a number of issues need to be addressed: 1) chemical and mechanical stabilities of many MOF sensors need to be increased; 2) more general approaches are needed to prepare MOF thin films of controlled thicknesses; 3) reliable methods are needed to integrate MOFs into other device structures to facilitate signal transduction and readout; 4) costs for MOF sensor production need to be minimized. Nevertheless, the area of chemical sensing with MOFs will continue to flourish and practically useful MOF sensors will appear in the near future.

In comparison to MOF sensors, NMOFs and NCPs are less explored for biological and biomedical imaging. They have been examined as contrast agents for MRI, CT, and optical imaging. The ability to readily tune compositions, particle sizes and morphologies, and surface functionalities makes NMOFs/NCPs a unique class of hybrid nanomaterials for biomedical applications, particularly in early diagnosis of cancer. NMOFs/NCPs are potentially advantageous over other inorganic nanoparticles owing to their intrinsic biodegrability of NMOFs/NCPs and the ability to use biocompatible building blocks. In addition, surface functionalization of NMOFs/NCPs with stealth coating and cell-targeting ligands should endow their long blood circulation and selective tumor targeting capabilities. The compositional and structural diversity of NMOFs/NCPs should also make it possible to co-deliver imagining contrast agents and chemotherapeutic drugs to provide real-time

monitoring of cargo delivery and tumor response to treatment. Significant efforts are needed to critically evaluate NMOFs/NCPs *in vivo* to establish pre-clinical guidelines on their efficacy and safety. NMOFs/NCPs are expected to have a bright future in biomedical imaging.

Acknowledgments

We thank NSF (DMR-0906662) and NIH-NCI (U01-CA151455) for financial support.

Reference

1. Ma L, Falkowski JM, Abney C, Lin W. Nat. Chem. 2010; 2:838–846. [PubMed: 20861899]
2. Lee J, Farha OK, Roberts J, Scheidt KA, Nguyen ST, Hupp JT. Chem. Soc. Rev. 2009; 38:1450–1459. [PubMed: 19384447]
3. Ma L, Abney C, Lin W. Chem. Soc. Rev. 2009; 38:1248–1256. [PubMed: 19384436]
4. Song F, Wang C, Falkowski JM, Ma L, Lin W. J. Am. Chem. Soc. 2010; 132:15390–15398. [PubMed: 20936862]
5. Wu C-D, Hu A, Zhang L, Lin W. J. Am. Chem. Soc. 2005; 127:8940–8941. [PubMed: 15969557]
6. Furukawa H, Ko N, Go YB, Aratani N, Choi SB, Choi E, Yazaydin AO, Snurr RQ, O'Keeffe M, Kim J, Yaghi OM. Science. 2010; 329:424–428. [PubMed: 20595583]
7. Ma L, Mihalcik DJ, Lin W. J. Am. Chem. Soc. 2009; 131:4610–4612. [PubMed: 19290636]
8. Murray LJ, Dinca M, Long JR. Chem. Soc. Rev. 2009; 38:1294–1314. [PubMed: 19384439]
9. Uemura K, Kitagawa S, Fukui K, Saito K. J. Am. Chem. Soc. 2004; 126:3817–3828. [PubMed: 15038736]
10. Evans OR, Lin W. Acc. Chem. Res. 2002; 35:511–522. [PubMed: 12118990]
11. Kent CA, Mehl BP, Ma L, Papanikolas JM, Meyer TJ, Lin W. J. Am. Chem. Soc. 2010; 132:12767–12769. [PubMed: 20735124]
12. Huxford RC, deKrafft KE, Boyle WS, Liu D, Lin W. Chem. Sci. 2012; 3:198–204.
13. Rieter WJ, Pott KM, Taylor KML, Lin W. J. Am. Chem. Soc. 2008; 130:11584–11585. [PubMed: 18686947]
14. Horcajada P, Chalati T, Serre C, Gillet B, Sebrie C, Baati T, Eubank JF, Heurtaux D, Clayette P, Kreuz C, Chang J-S, Hwang YK, Marsaud V, Bories P-N, Cynober L, Gil S, Ferey G, Couvreur P, Gref R. Nat. Mater. 2010; 9:172–178. [PubMed: 20010827]
15. Chen Z, Lu C. Sens. Lett. 2005; 3:274–295.
16. Li J, Lu Y, Ye Q, Cinke M, Han J, Meyyappan M. Nano Lett. 2003; 3:929–933.
17. Kolmakov A, Moskovits M. Annu. Rev. Mater. Res. 2004; 34:151–180.
18. Thakar R, Chen Y, Snee PT. Nano Lett. 2007; 7:3429–3432. [PubMed: 17927260]
19. Burns A, Sengupta P, Zedayko T, Baird B, Wiesner U. Small. 2006; 2:723–726. [PubMed: 17193111]
20. Kong J, Franklin NR, Zhou C, Chapline MG, Peng S, Cho K, Dai H. Science. 2000; 287:622–625. [PubMed: 10649989]
21. Heath JR, Davis ME. Annu. Rev. Med. 2008; 59:251–265. [PubMed: 17937588]
22. Cheng MM-C, Cuda G, Bunimovich YL, Gaspari M, Heath JR, Hill HD, Mirkin CA, Nijdam AJ, Terracciano R, Thundat T, Ferrari M. Curr. Opin. Chem. Biol. 2006; 10:11–19. [PubMed: 16418011]
23. Sun Y, Rogers JA. Adv. Mater. 2007; 19:1897–1916.
24. Shipway AN, Katz E, Willner I. ChemPhysChem. 2000; 1:18–52. [PubMed: 23696260]
25. Lin P, Yan F. Adv. Mater. 2012; 24:34–51. [PubMed: 22102447]
26. Mabeck J, Malliaras G. Anal. Bioanal. Chem. 2006; 384:343–353. [PubMed: 16079978]
27. Yavuz MS, Cheng Y, Chen J, Cobley CM, Zhang Q, Rycenga M, Xie J, Kim C, Song KH, Schwartz AG, Wang LV, Xia Y. Nat. Mater. 2009; 8:935–939. [PubMed: 19881498]

28. Lee JE, Lee N, Kim H, Kim J, Choi SH, Kim JH, Kim T, Song IC, Park SP, Moon WK, Hyeon T. J. Am. Chem. Soc. 2010; 132:552–557. [PubMed: 20017538]
29. Cheon J, Lee J-H. Acc. Chem. Res. 2008; 41:1630–1640. [PubMed: 18698851]
30. Peer D, Karp JM, Hong S, Farokhzad OC, Margalit R, Langer R. Nat. Nanotechnol. 2007; 2:751–760. [PubMed: 18654426]
31. Fang J, Nakamura H, Maeda H. Adv. Drug Del. Rev. 2011; 63:136–151.
32. Ferrari M. Nat. Rev. Cancer. 2005; 5:161–171. [PubMed: 15738981]
33. Kamaly N, Xiao Z, Valencia PM, Radovic-Moreno AF, Farokhzad OC. Chem. Soc. Rev. 2012; 41:2971–3010. [PubMed: 22388185]
34. Kent CA, Liu D, Meyer TJ, Lin W. J. Am. Chem. Soc. 2012; 134:3991–3994. [PubMed: 22329430]
35. Lu G, Hupp JT. J. Am. Chem. Soc. 2010; 132:7832–7833. [PubMed: 20486704]
36. Lin W, Rieter WJ, Taylor KML. Angew. Chem. Int. Ed. 2009; 48:650–658.
37. Oh M, Mirkin CA. Angew. Chem. Int. Ed. 2006; 45:5492–5494.
38. Lan A, Li K, Wu H, Olson David H, Emge Thomas J, Ki W, Hong M, Li J. Angew. Chem. Int. Ed. 2009; 48:2334–2338.
39. Chen B, Wang L, Xiao Y, Fronczek Frank R, Xue M, Cui Y, Qian G. Angew. Chem. Int. Ed. 2009; 48:500–503.
40. Jiang Y-Y, Ren S-K, Ma J-P, Liu Q-K, Dong Y-B. Chem. Eur. J. 2009; 15:10742–10746. [PubMed: 19746367]
41. Chen B, Wang L, Zapata F, Qian G, Lobkovsky EB. J. Am. Chem. Soc. 2008; 130:6718–6719. [PubMed: 18452294]
42. Xie Z, Ma L, deKrafft KE, Jin A, Lin W. J. Am. Chem. Soc. 2010; 132:922–923. [PubMed: 20041656]
43. Qi X-L, Lin R-B, Chen Q, Lin J-B, Zhang J-P, Chen X-M. Chem. Sci. 2011; 2:2214–2218.
44. Qi X-L, Liu S-Y, Lin R-B, Liao P-Q, Ye J-W, Lai Z, Guan Y, Cheng X-N, Zhang J-P, Chen X-M. Chem. Commun. 2013; 49:6864–6866.
45. Takashima Y, Martínez VM, Furukawa S, Kondo M, Shimomura S, Uehara H, Nakahama M, Sugimoto K, Kitagawa S. Nat. Commun. 2011; 2:168–000. [PubMed: 21266971]
46. Wanderley MM, Wang C, Wu C-D, Lin W. J. Am. Chem. Soc. 2012; 134:9050–9053. [PubMed: 22607498]
47. Siegel R, Naishadham D, Jemal A. CA-Cancer J. Clin. 2013; 63:11–30. [PubMed: 23335087]
48. Choi KY, Liu G, Lee S, Chen X. Nanoscale. 2012; 4:330–342. [PubMed: 22134683]
49. Davis ME, Chen Z, Shin DM. Nat. Rev. Drug Discov. 2008; 7:771–782. [PubMed: 18758474]
50. Della Rocca J, Liu D, Lin W. Acc. Chem. Res. 2011; 44:957–968. [PubMed: 21648429]
51. Taylor-Pashow KML, Della Rocca J, Xie Z, Tran S, Lin W. J. Am. Chem. Soc. 2009; 131:14261–14263. [PubMed: 19807179]
52. Rieter WJ, Taylor KML, An H, Lin W, Lin W. J. Am. Chem. Soc. 2006; 128:9024–9025. [PubMed: 16834362]
53. Taylor Kathryn ML, Jin A, Lin W. Angew. Chem. Int. Ed. 2008; 47:7722–7725.
54. Taylor KML, Rieter WJ, Lin W. J. Am. Chem. Soc. 2008; 130:14358–14359. [PubMed: 18844356]
55. deKrafft KE, Xie Z, Cao G, Tran S, Ma L, Zhou OZ, Lin W. Angew. Chem. Int. Ed. 2009; 48:9901–9904.
56. Horcajada P, Serre C, Vallet-Regí M, Sebban M, Taulelle F, Férey G. Angew. Chem. Int. Ed. 2006; 45:5974–5978.
57. Horcajada P, Serre C, Maurin G, Ramsahye NA, Balas F, Vallet-Regí Ma, Sebban M, Taulelle F, Férey Gr. J. Am. Chem. Soc. 2008; 130:6774–6780. [PubMed: 18454528]
58. An J, Geib SJ, Rosi NL. J. Am. Chem. Soc. 2009; 131:8376–8377. [PubMed: 19489551]
59. Zou H, Wu S, Shen J. Chem. Rev. 2008; 108:3893–3957. [PubMed: 18720998]
60. Lu Y, Yin Y, Mayers BT, Xia Y. Nano Lett. 2002; 2:183–186.

61. Rieter WJ, Taylor KML, Lin W. J. Am. Chem. Soc. 2007; 129:9852–9853. [PubMed: 17645339]
62. Zhao D, Tan S, Yuan D, Lu W, Rezenom YH, Jiang H, Wang L-Q, Zhou H-C. Adv. Mater. 2011; 23:90–93. [PubMed: 20972982]
63. Liu D, Kramer SA, Huxford-Phillips RC, Wang S, Della Rocca J, Lin W. Chem. Commun. 2012; 48:2668–2670.
64. Baati T, Njim L, Neffati F, Kerkeni A, Bouttemi M, Gref R, Najjar MF, Zakhama A, Couvreur P, Serre C, Horcajada P. Chem. Sci. 2013; 4:1597–1607.
65. deKrafft KE, Boyle WS, Burk LM, Zhou OZ, Lin W. J. Mater. Chem. 2012; 22:18139–18144. [PubMed: 23049169]
66. Liu D, Huxford RC, Lin W. Angew. Chem. Int. Ed. 2011; 50:3696–3700.
67. Nishiyabu R, Hashimoto N, Cho T, Watanabe K, Yasunaga T, Endo A, Kaneko K, Niidome T, Murata M, Adachi C, Katayama Y, Hashizume M, Kimizuka N. J. Am. Chem. Soc. 2009; 131:2151–2158. [PubMed: 19166341]

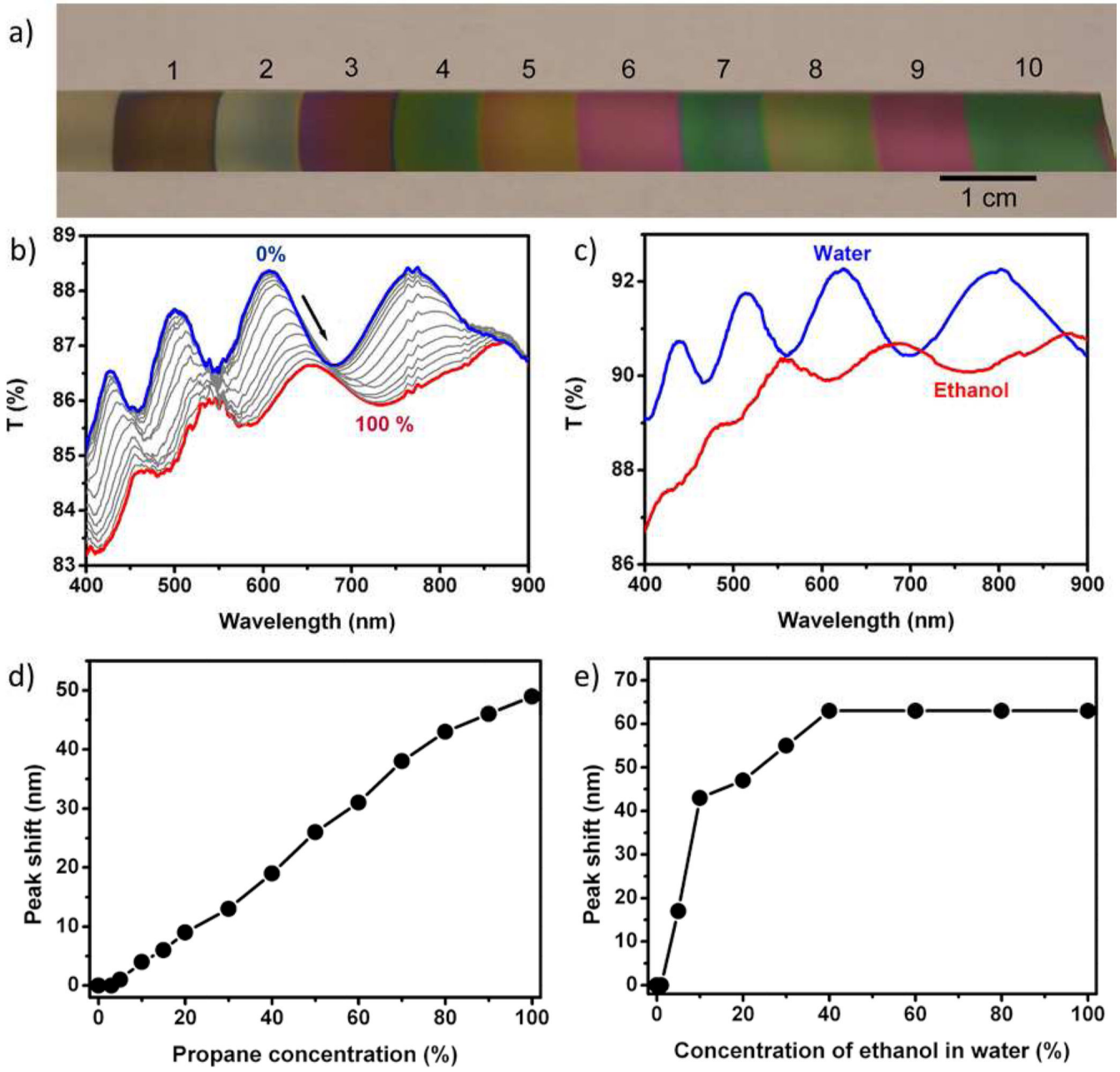

Figure 1.

(a) Photograph of a series of ZIF-8 films of various thicknesses grown on silicon substrates. UV-vis transmission spectra of ZIF-8 film on glass after exposure to (b) propane vapor of various concentrations from 0% (blue) to 100% (red) and (c) ethanol (red) or water (blue) and corresponding interference peak (originally at 612 nm) shift versus (d) propane concentration in N_2 diluent and (e) ethanol concentration (v/v %) in ethanol/water solutions. Copyright 2010 American Chemistry Society.

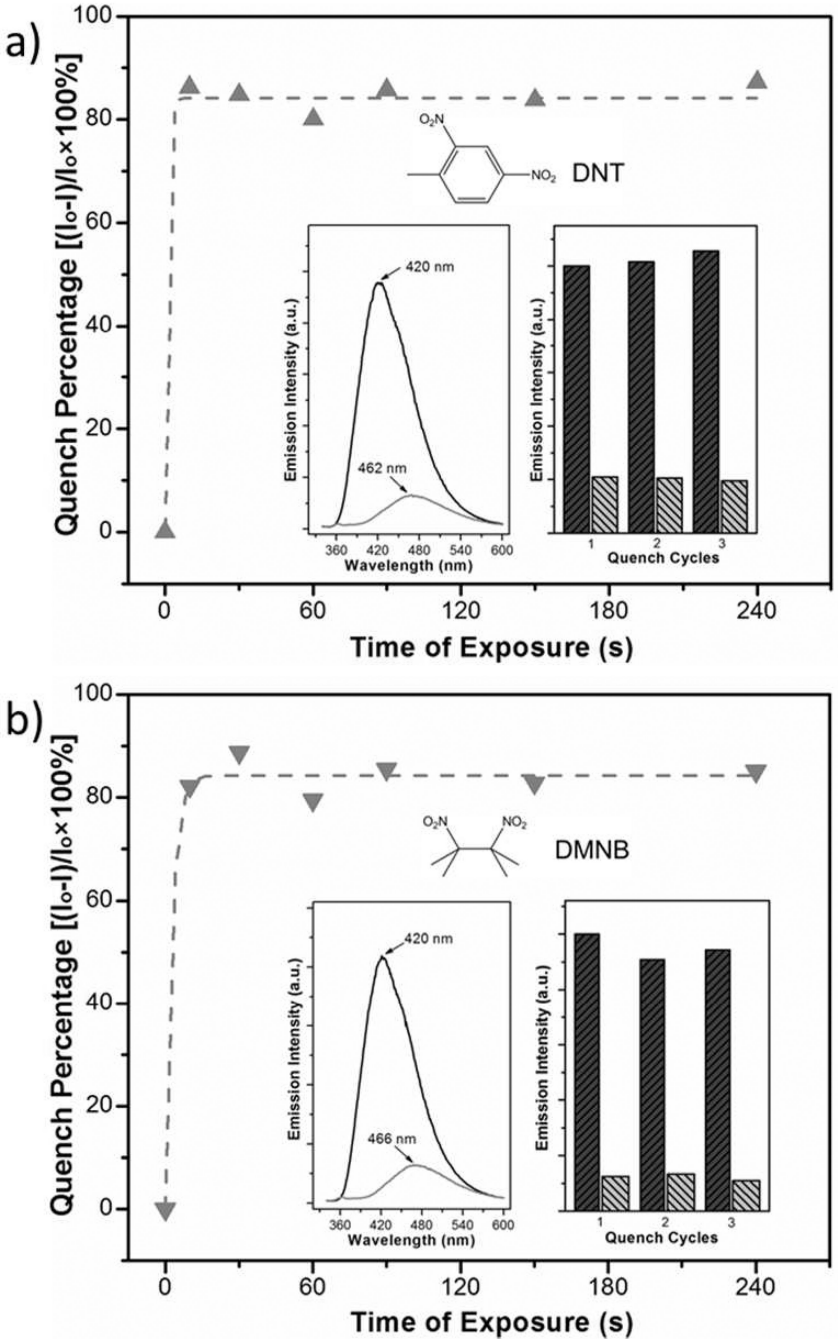

Figure 2.

Time-dependent fluorescence quenching by (a) DNT and (b) DMNB (excitation wavelength=320 nm). Insets: the corresponding fluorescence spectra before and after exposure to the analyte vapors for 10 s (left) and three consecutive quench/regeneration cycles (right). Copyright 2009 Wiley-VCH.

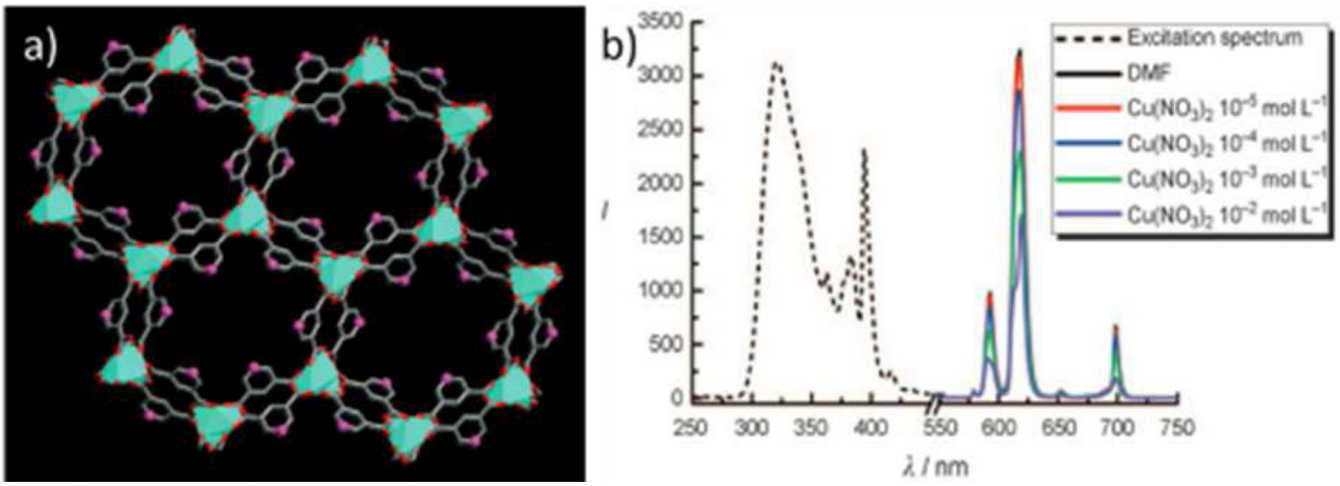

Figure 3.

(a) Crystal structure of the Eu-pdc MOF, viewed along the *a* axis. (b) The excitation and PL spectra of MOF activated in DMF solutions of $Cu(NO_3)_2$ at different concentrations (excited and monitored at 321 nm and 618 nm, respectively). Copyright 2009 Wiley-VCH.

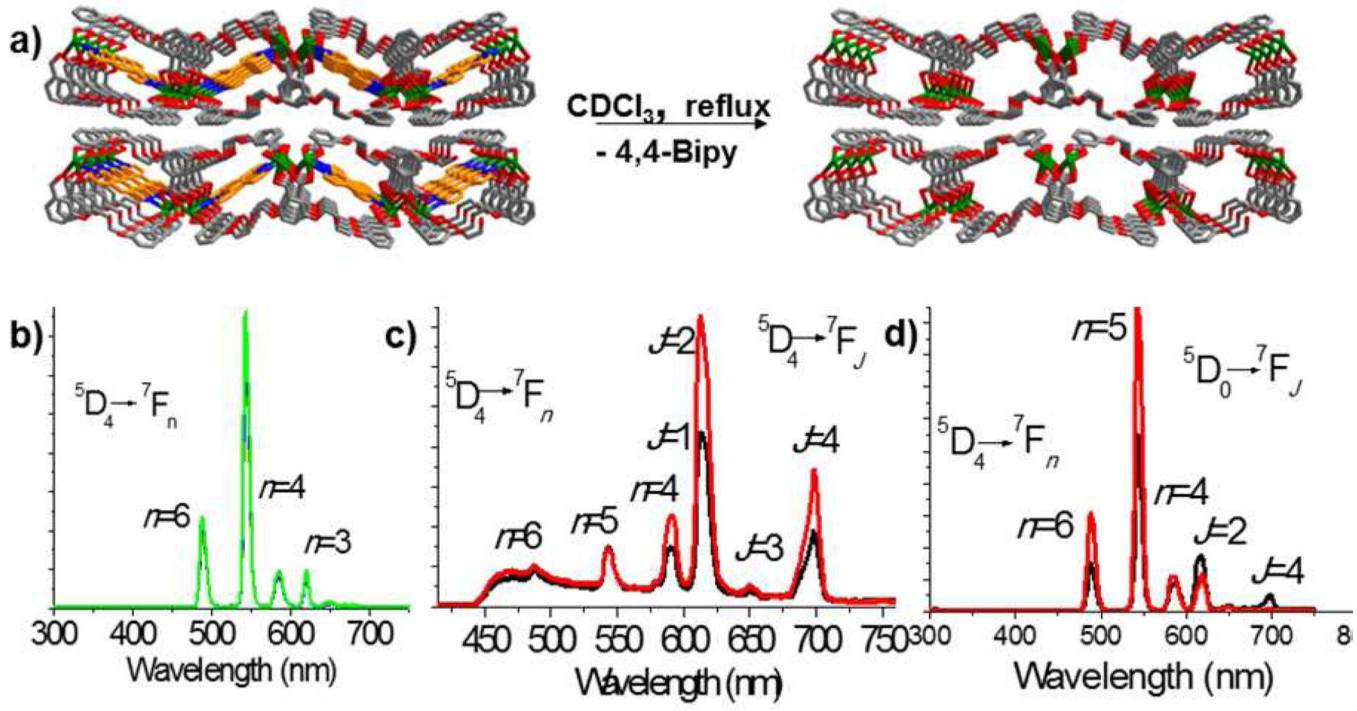

Figure 4.

(a) Schematic showing the formation of $[Pb_2(bco)_2]$ by leaching of the weakly coordinating bipy. The cation encapsulation and exchange experiments give the emission spectra of (b) after stirring $[Pb_2(bco)_2]$ in $Tb(ClO_4)_3$ aqueous solution for 3h; (c) sample of (b) stirred in $Eu(ClO_4)_3$ aqueous solution at one (black) and two (red) days; (d) sample of (c) stirred in $Tb(ClO_4)_3$ aqueous solution at one (black) and two (red) days. Excitation are all at 303 nm.

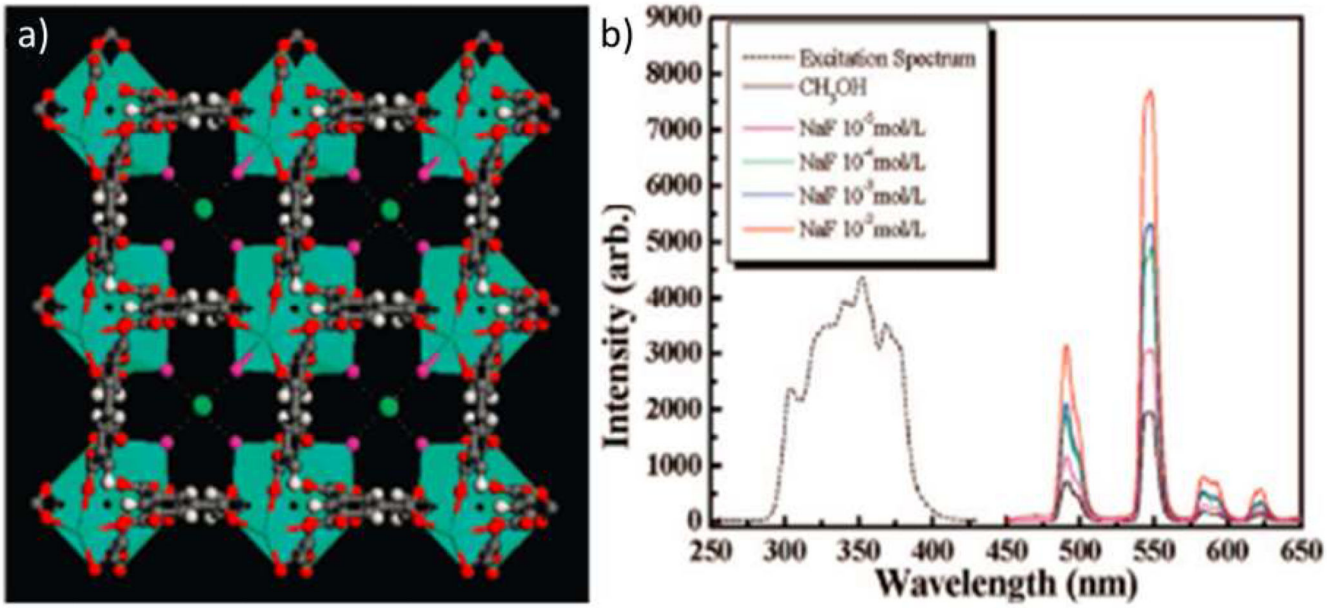

Figure 5.

(a) Single crystal X-ray structure of Tb(BTC) MOF activated in methanol containing NaF. (b) Excitation (dotted) and PL spectra (solid) of the Tb(BTC) MOF activated in different concentrations of NaF. Copyright 2008 American Chemistry Society.

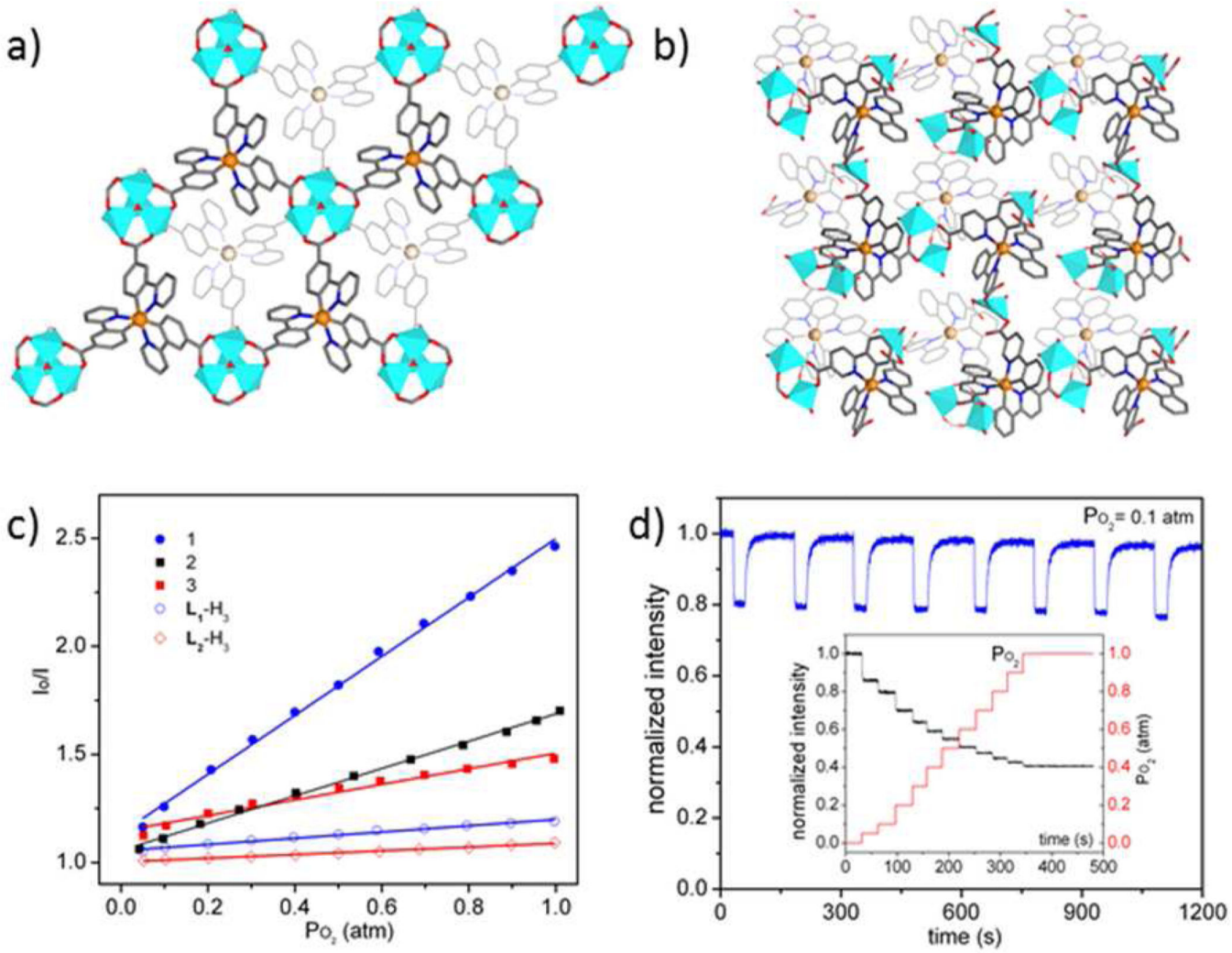

Figure 6.

Top view of the 2D bilayer structure of the MOFs synthesized from two $Ir(ppy)_3$-derived ligands (a, b); (c) Stern-Volmer plot showing I_0/I vs O_2 partial pressure for ligand complexes and MOFs; (d) Reversible quenching of phosphorescence of the MOF upon alternating exposure to 0.1 atm O_2 and application of vacuum. The inset shows rapid equilibration of phosphorescence of the MOF after each dose of O_2. Copyright 2010 American Chemistry Society.

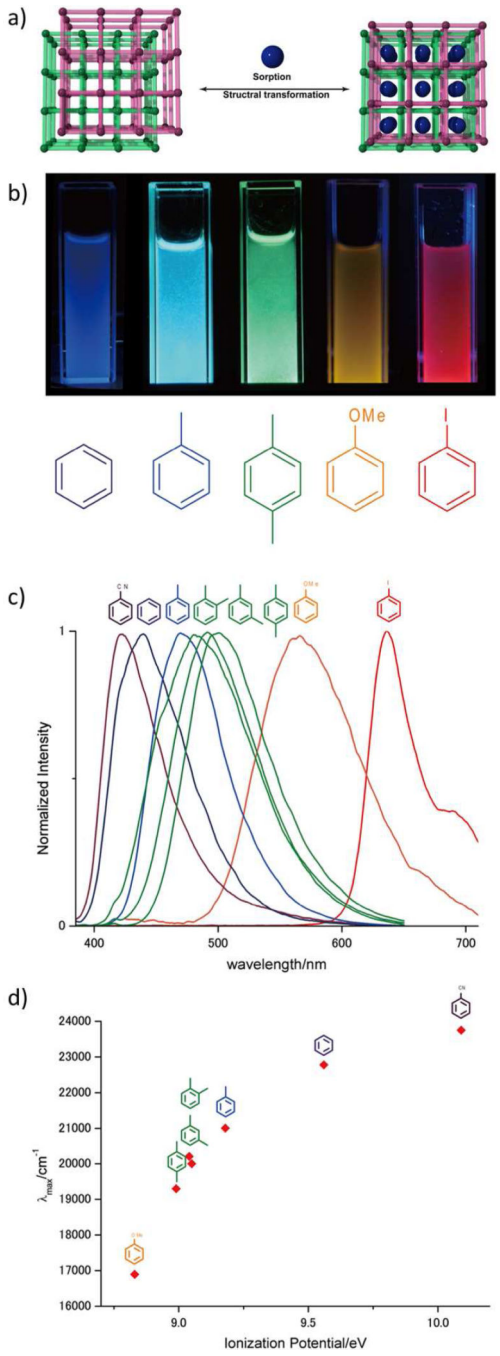

Figure 7.

(a) Schematic depiction of space flexibility in entangled MOF for molecular decoding. (b) The resulting luminescence of MOF powders suspension in organic liquid indicated, with 365 nm irradiation. (c) Normalized luminescent spectra of guest-containing MOFs upon excitation at 370 nm. (d) The relationship between the emission energy of guest-containing MOF and the ionization potential of each guest molecules. Copyright 2011 Nature Publishing Group.

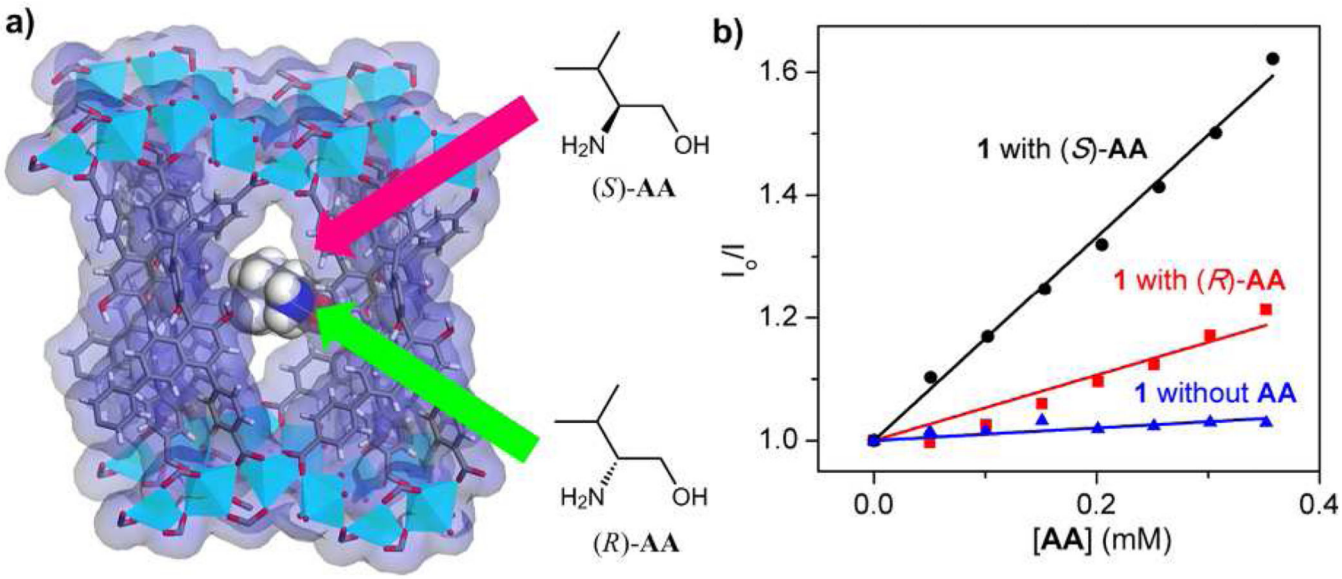

Figure 8.

a) Schematic showing chiral sensing of amino alcohols with a Cd MOF with BINOL-derived tetracarboxylate ligand. b) Stern-Völmer plots of fluorescence quenching of the Cd MOF by (*R*)- and (*S*)-2-amino-3-methyl-1-butanol (AA). Copyright 2012 American Chemical Society.

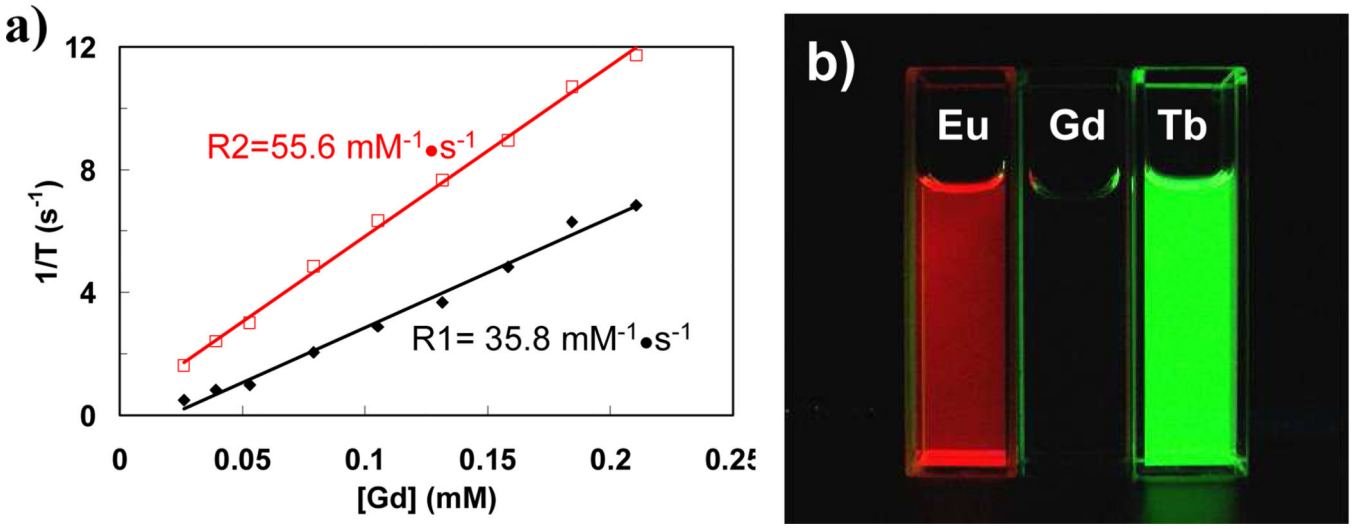

Figure 9.

(a) *r*1 and *r*2 relaxivity curves of $Gd(BDC)_{1.5}(H_2O)_2$ of ~100 nm in length by ~40 nm in diameter. In comparison, OmniScan gave an *r*1 of 4.1 $mM^{-1}s^{-1}$ under these conditions. (b) Luminescence images of ethanolic suspensions of Eu- and Tb-doped $Gd(BDC)_{1.5}(H_2O)_2$ when irradiated with UV light. Copyright 2006 American Chemical Society.

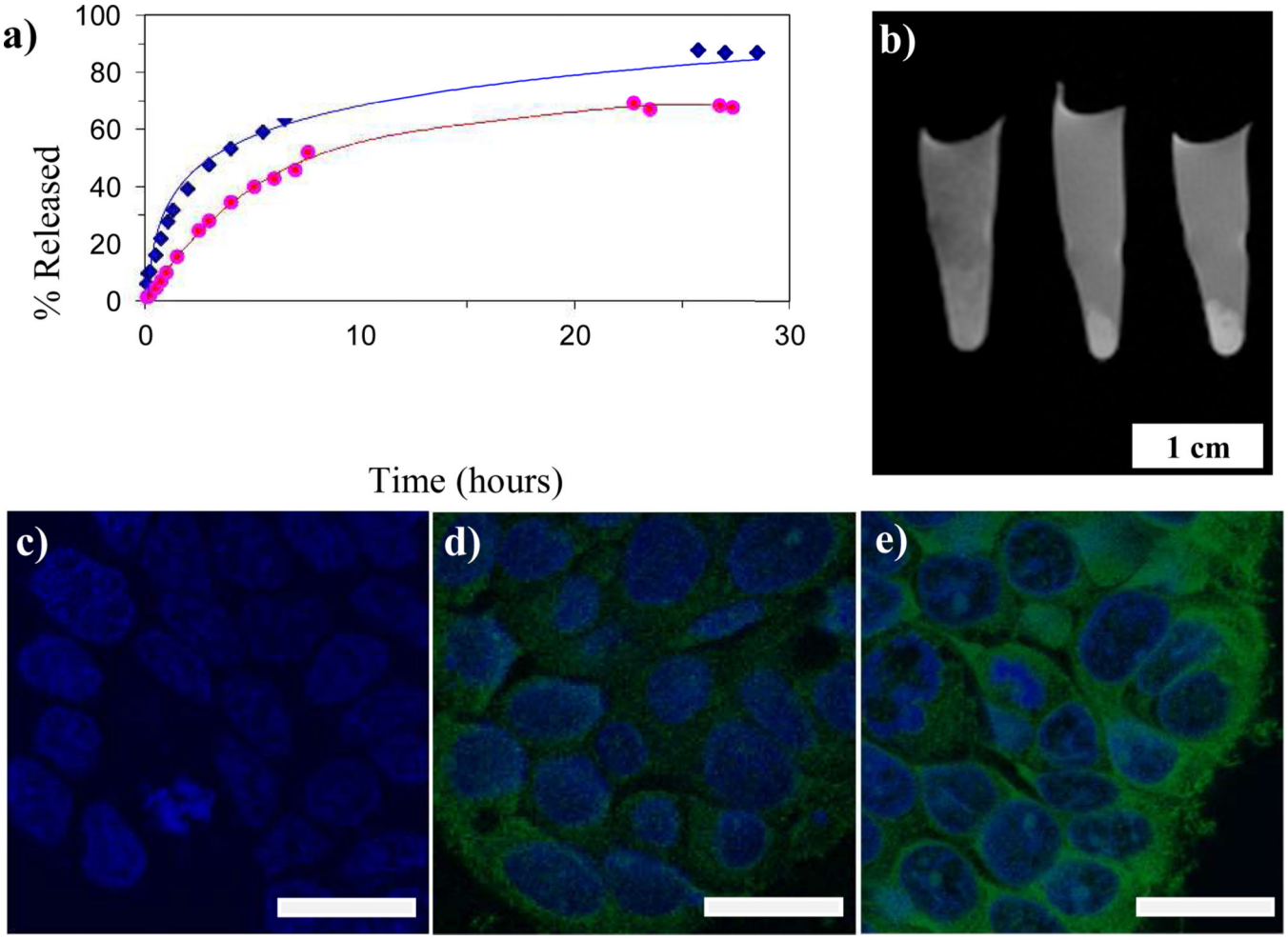

Figure 10.

(a) Dissolution curves of uncoated (blue) and silica-coated (red) $Mn_3(BTC)_2(H_2O)_6$ nanoparticles ($Mn@SiO_2$) in water at 37 °C (% released vs time). (b) *In vitro* MR images of HT-29 cells incubated with no particle (left), nontargeted $Mn@SiO_2$ (middle), and c(RGDfK)-targeted $Mn@SiO._2$ (right). (c–e) Merged confocal images of HT-29 cells that were incubated with no particles (c), nontargeted $Mn@SiO_2$ (d), c(RGDfK)-targeted $Mn@SiO_2$ (e). The blue color was from DRAQ5 used to stain the cell nuclei while the green color was from rhodamine B. The bars represent 20 μm. Copyright 2008 American Chemical Society.

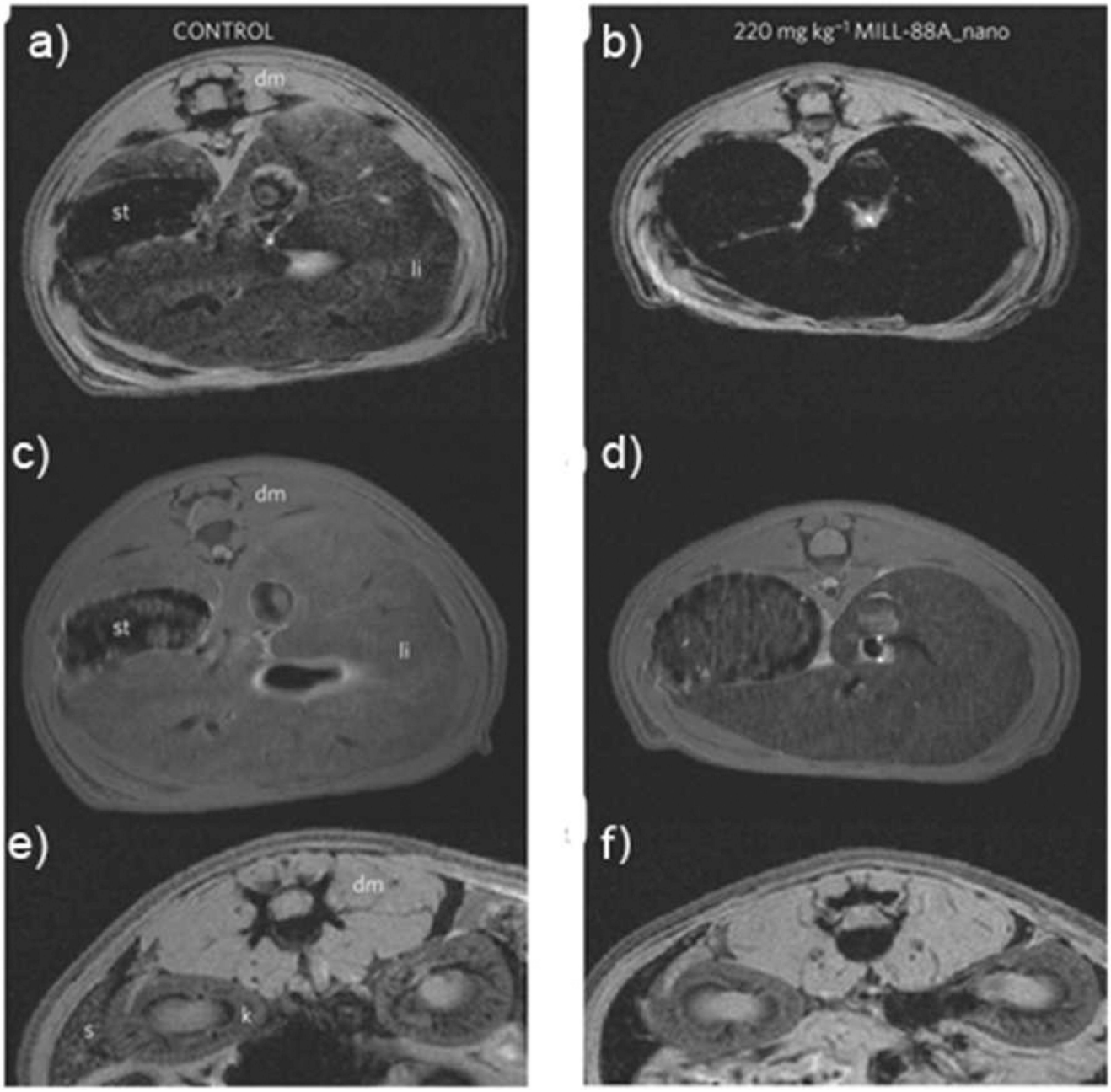

Figure 11.

T_2 weighted MR images of Wistar rats injected with no particle (a,c,e) or 220 mg/kg MIL-88A (e,d,f). The images were acquired using either gradient echo (a,b,e,f) or spin echo (c,d) sequences. The images show the liver (a–d) or spleen (e,f) regions 30 minutes post-injection. [dm=dorsal muscle, k=kidney, li=liver, s=spleen, st=stomach]. Reproduced with permission from reference [14]. Copyright Nature Publishing Group 2010.

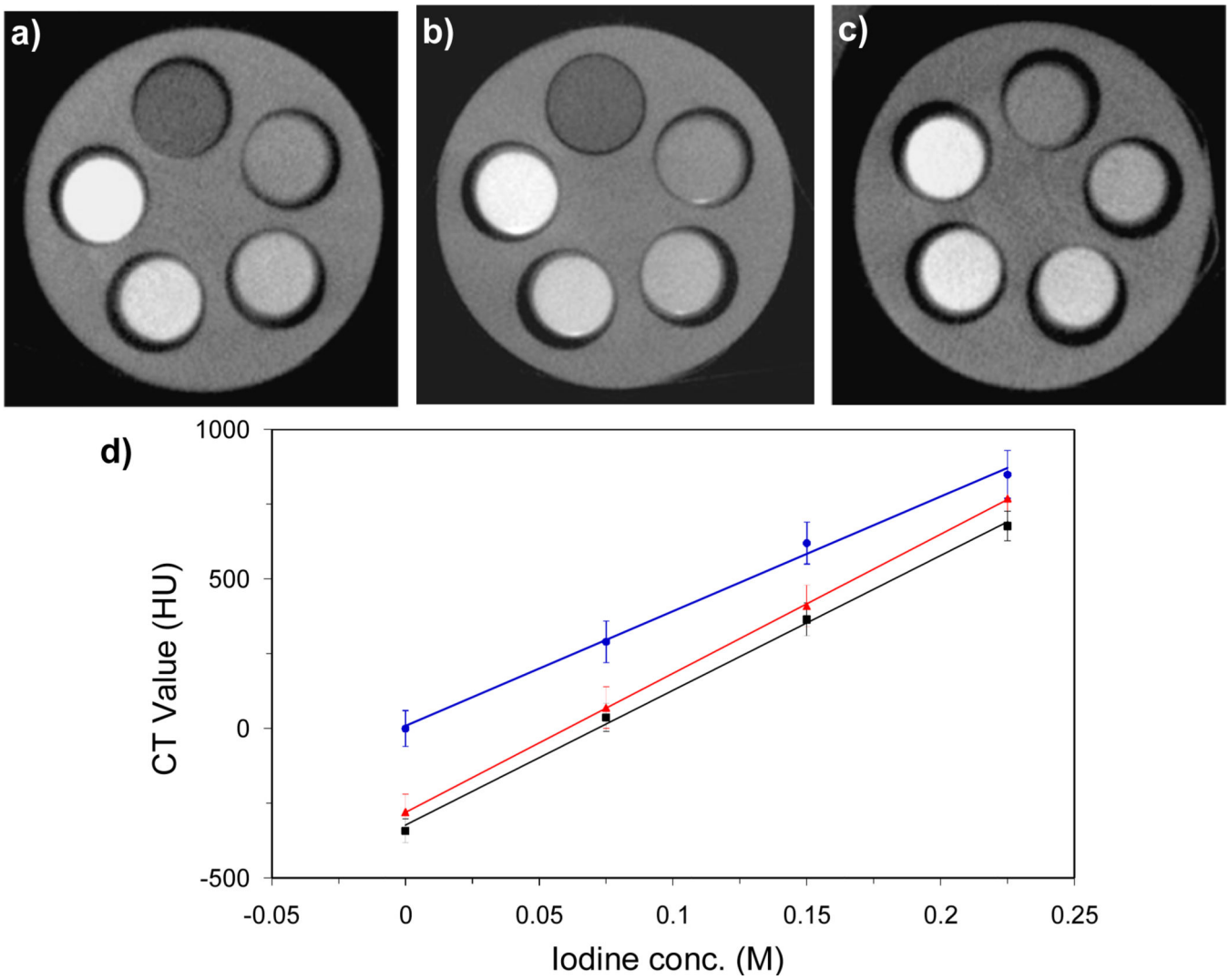

Figure 12.

CT phantom images of a) $[Cu(I_4\text{-BDC})(H_2O)_2]\cdot 2H_2O$ (NCP 3a) and b) $[Zn(I_4\text{-BDC})(EtOH)_2]\cdot 2EtOH$ (NCP 5b) dispersed in ethanol, and c) Iodixanol in aqueous solution. From the top, clockwise, the slots have [I]=0, 0.075, 0.150, 0.225, and 0.300 M. d) Xray attenuation as a function of [I] for NCP 3a at 40 kVp, NCP 5b at 50 kVp, and Iodixanol at 40 kVp. Blue: Iodixanol, Red: NCP 3a, Black: 5b. Copyright 2009 Wiley-VCH.

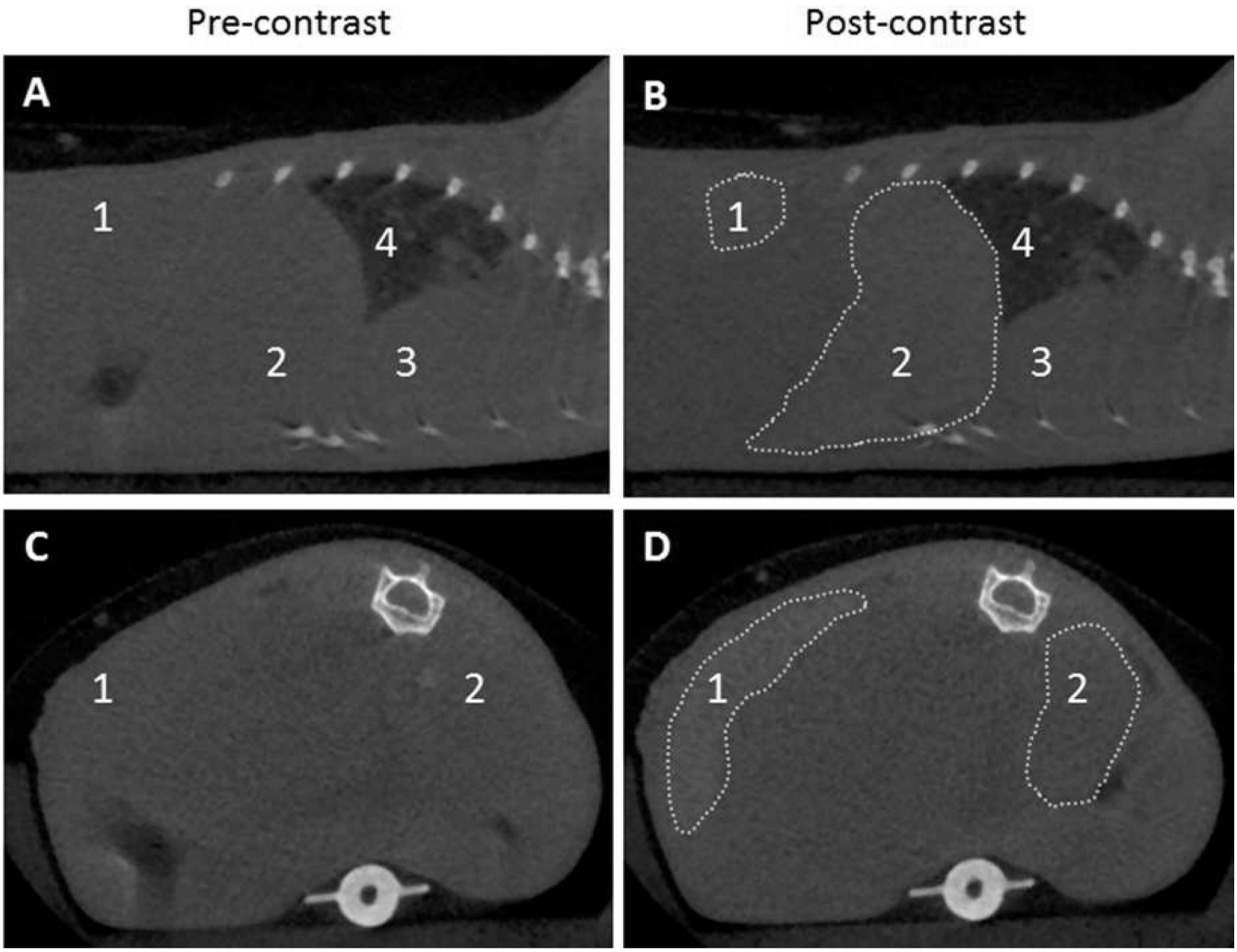

Figure 13.

(A and B) Sagittal and (C and D) axial CT slices of a mouse pre-contrast and 15 min after injection of Hf-UiO@SiO_2@PEG. The areas of increased attenuation are outlined, and the labels are: 1 – spleen (+131 HU), 2 – liver (+86 HU), 3 – heart, and 4 – lungs. Copyright 2012 Royal Society of Chemistry.

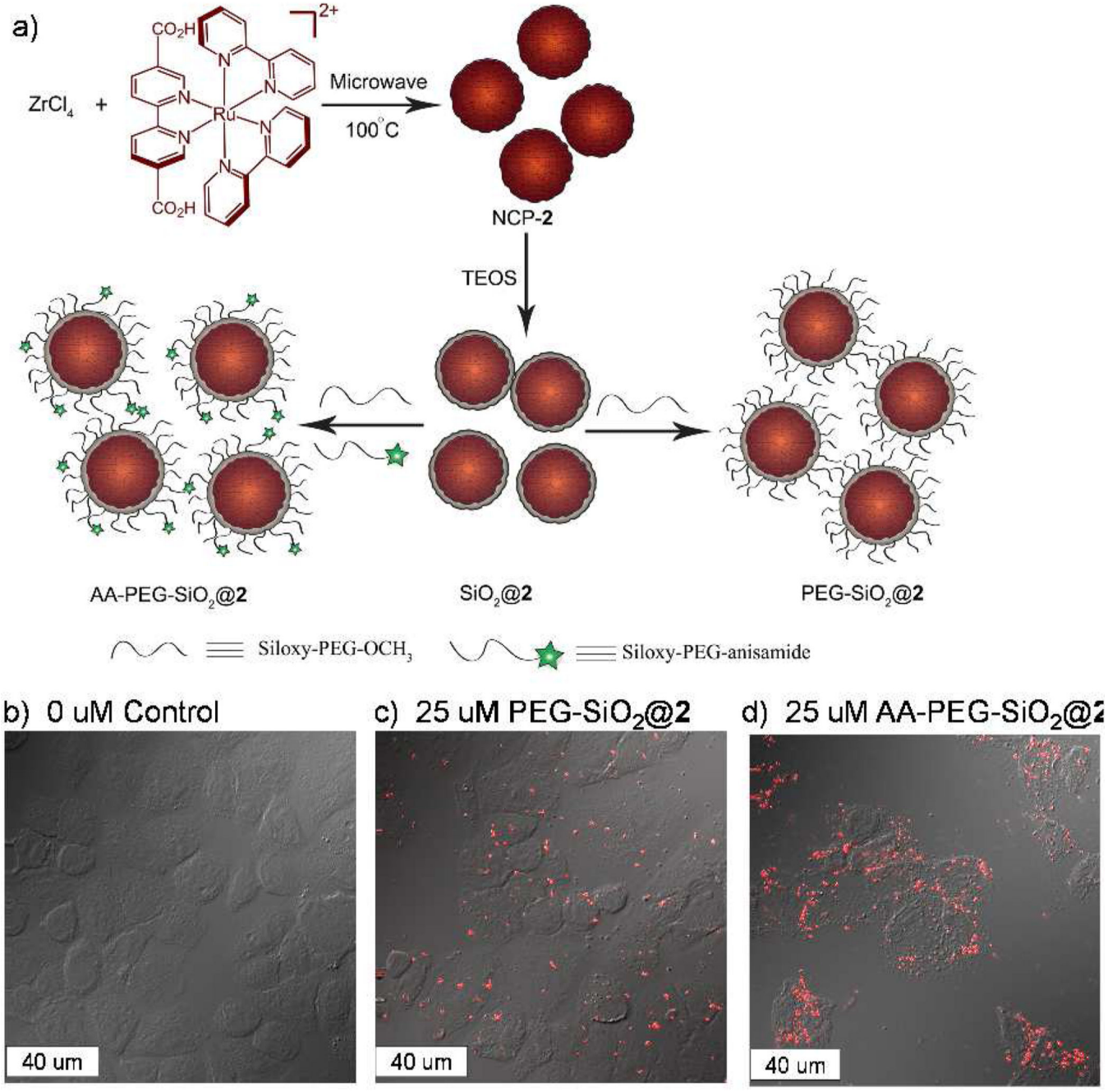

Figure 14.

a) Synthesis of Zr NCP, coating of Zr NCP with silica, and further functionalization with PEG and PEG-anisamide. Confocal microscopic images of H460 cells that have been incubated with various nanoparticles: control cells without any particles (b), cells with **Zr-NCP**@PEG-SiO_2(c), and cells with **Zr-NCP**@AA-PEG-SiO_2 (d). Copyright 2011 Wiley-VCH.

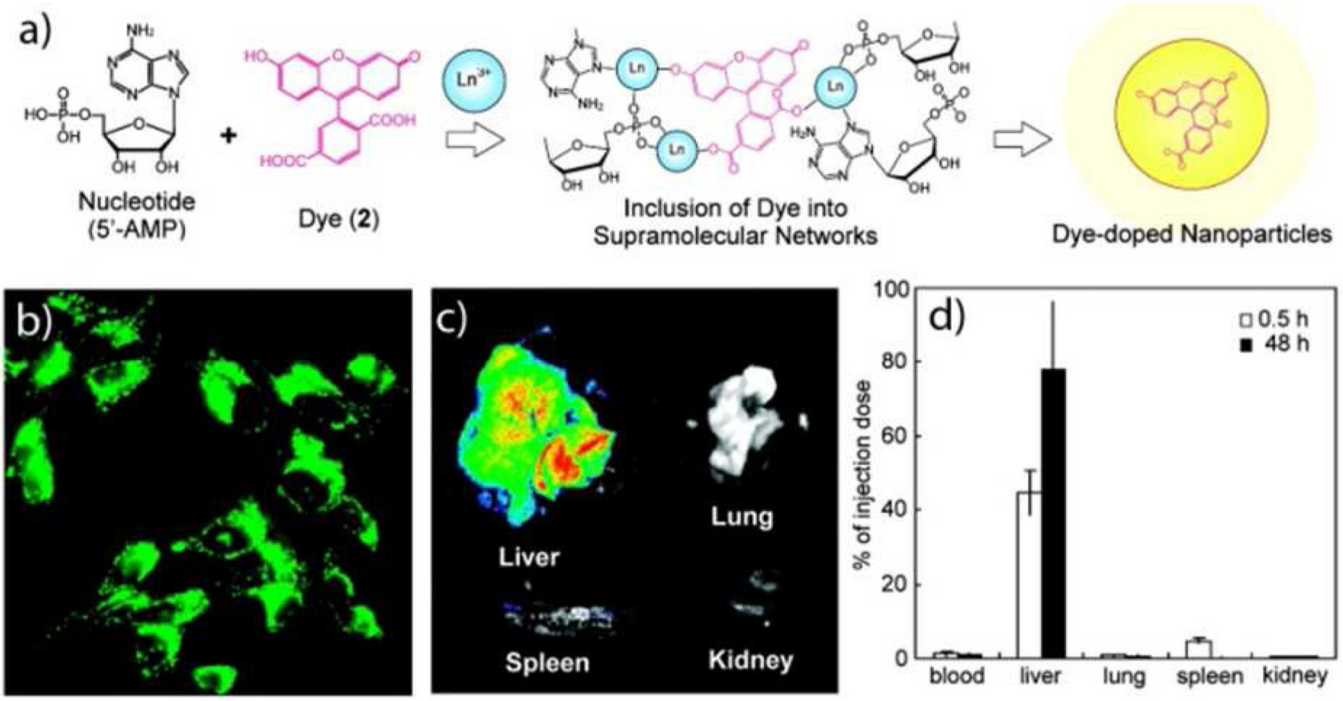

Figure 15.

a) Schematic representation of the incorporation of anionic dyes within supramolecular networks. b) Fluorescence microscopy image of HeLa cells incubated with 4-doped 5'-AMP/Gd^{3+} NPs. c) Fluorescent images of organs from mice injected with 4-doped 5'-AMP/Gd^{3+} NPs. d) Biodistribution of 4-doped 5'-AMP/Gd^{3+} NPs in mice at 0.5 h and 48 h post-injection time point. Copyright 2009 American Chemical Society.

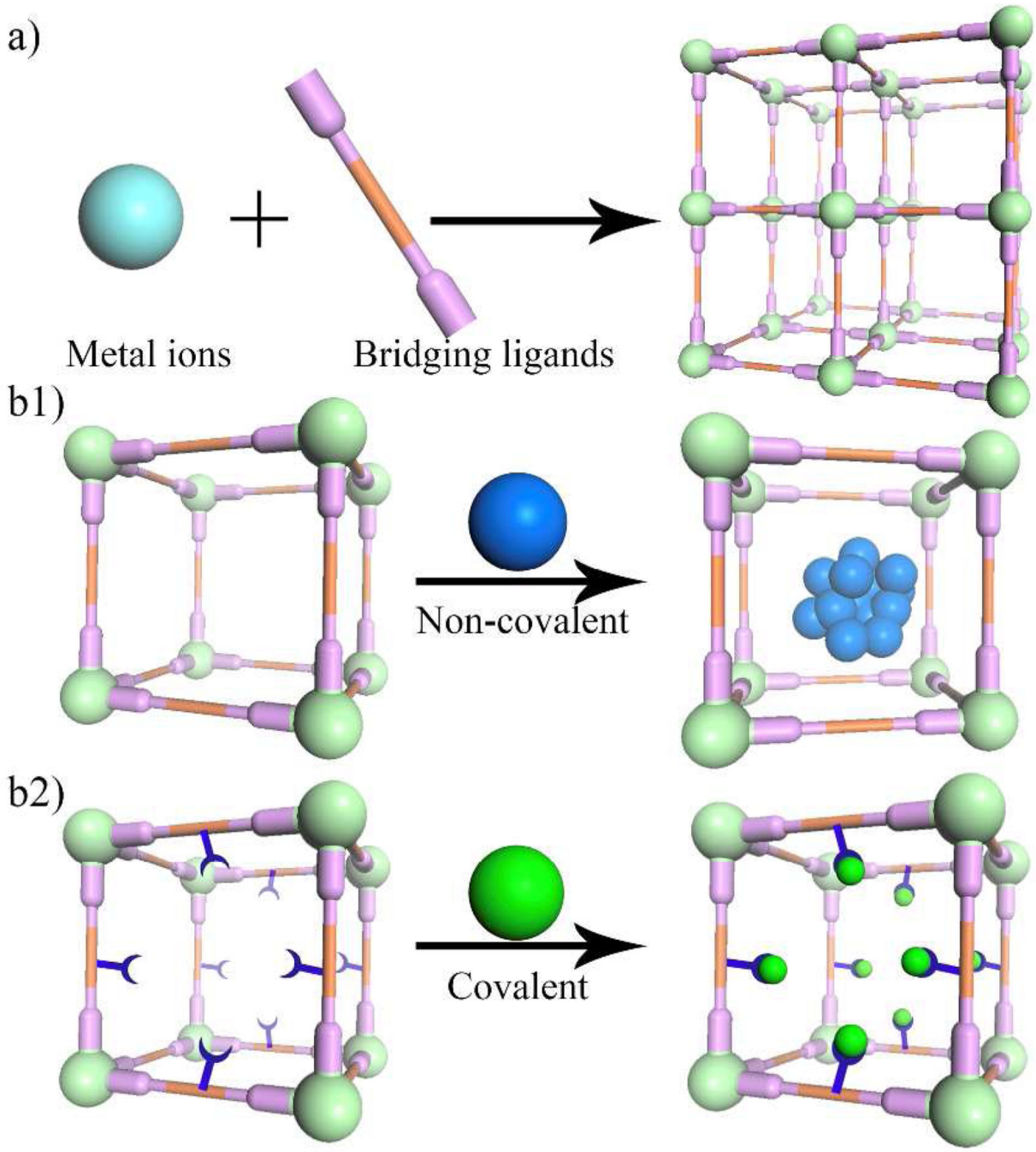

Scheme 1.

Schematic representations of direct incorporation of biomedically relevant agents into the MOF framework (a) and cargo loading by non-covalent (b1) and covalent (b2) means.